Impacts of Emergent Vegetation on Hyporheic Exchange

Qingjun Judy Yang[1] and Shih-Hsun Huang[2]

[1]University of Minnesota
[2]National Taiwan University

November 23, 2022

Abstract

Hyporheic exchange, or the exchange of water and solutes between surface and subsurface water at the sediment-water interface, regulates water quality and biogeochemical cycles in aquatic ecosystems. Vegetation, which is ubiquitous in nature, is known to impact hyporheic exchange, yet how vegetation impacts hyporheic exchange remains to be characterized. Here, we show that at the same spatially and temporally averaged flow velocity U, vegetation increases the rate of hyporheic exchange by a factor of four. By tracking the movement of fluorescent dye in a flume with index-matched sediment and translucent vegetation dowels, we demonstrate that vegetation-induced hyporheic exchange at the sediment-water interface can be characterized by an effective hyporheic exchange velocity, V_H. We further demonstrate that V_H could correlate with the total near-bed turbulent kinetic energy k_t rather than U. A k_t-based model was developed to characterize the impacts of vegetation on hyporheic exchange.

Impacts of Emergent Vegetation on Hyporheic Exchange

S. Huang[1,2], and J. Q. Yang[1,2]

[1] Saint Anthony Falls Laboratory, University of Minnesota, Minneapolis, MN 55414.

[2] Department of Civil, Environmental, and Geo-Engineering, University of Minnesota, Minneapolis, MN 55455.

Corresponding author: J. Q. Yang (judyyang@umn.edu)

Key Points:

- Emergent vegetation increases the exchange of solutes between surface and subsurface water in the hyporheic zone.
- Vegetation-induced hyporheic exchange can be characterized by the first-order equations with an effective hyporheic exchange velocity.
- The effective velocity of the vegetation-induced hyporheic exchange scale as the total near-bed turbulent kinetic energy k_t.

Abstract

Hyporheic exchange, or the exchange of water and solutes between surface and subsurface water at the sediment-water interface, regulates water quality and biogeochemical cycles in aquatic ecosystems. Vegetation, which is ubiquitous in nature, is known to impact hyporheic exchange, yet how vegetation impacts hyporheic exchange remains to be characterized. Here, we show that at the same spatially and temporally averaged flow velocity U, vegetation increases the rate of hyporheic exchange by a factor of four. By tracking the movement of fluorescent dye in a flume with index-matched sediment and translucent vegetation dowels, we demonstrate that vegetation-induced hyporheic exchange at the sediment-water interface can be characterized by an effective hyporheic exchange velocity, V_H. We further demonstrate that V_H could correlate with the total near-bed turbulent kinetic energy k_t rather than mean flow velocity U when $k_t < 6 \times 10^{-4}$ $\mathrm{m^2/s^2}$. A k_t-based model was developed to characterize the impacts of vegetation on hyporheic exchange.

Plain Language Summary

The exchange of contaminants and nutrients between surface- and subsurface-water in the hyporheic zone of rivers and wetlands controls water quality as well as the metabolism of benthic microbes and the associated biogeochemical cycles. Vegetation, which is ubiquitous in aquatic ecosystems, has been found to affect the surface- and subsurface-exchange and as such impact water quality and stream biogeochemical cycles. However, how vegetation impacts this exchange remains unclear, making it difficult to predict the contaminant transport and biogeochemical cycles in streams, lakes, and coastal areas with vegetation. In this study, we directly visualized the release of fluorescent dye from the transparent sediment into the surface water in a water-recirculating tank filled with translucent vegetation. We discovered that vegetation can significantly increase the exchange in the hyporheic zone. Furthermore, we proposed a model to predict the impacts of the vegetation on hyporheic exchange. We believe this finding will help improve predictions of contaminant transport and biogeochemical cycles in streams and other aquatic ecosystems. The results of this study will also help ecologists design stream restoration projects that use vegetation to increase the retention and degradation of contaminants in sediment.

1 Introduction

Hyporheic zone is often referred to the region of saturated sediments underneath the surface water of a stream, where water, gases, nutrients, and contaminants are consistently being exchanged (Boano et al., 2014; Boulton et al., 1998; Gooseff, 2010). The exchange between surface and subsurface water supplies nutrients and oxygen to underground microbes and as such controls the biogeochemical cycles and biodiversity of stream bed (Battin et al., 2008; Jones Jr & Holmes, 1996; Tonina & Buffington, 2009; Wohl, 2016). The exchange in hyporheic zone also determines the retention and degradation of contaminants in stream (Grant et al., 2014; Lewandowski et al., 2011; McCallum et al., 2020). Fundamental understanding of the exchange in hyporheic zone is critical for predicting the biogeochemical cycles, biodiversity, and fate of contaminants in streams.

Over the past decades, extensive studies have been conducted to characterize the impacts of channel morphology such as bedforms (Buffington & Tonina, 2009; Dudunake et al., 2020; Marion et al., 2002; Packman et al., 2004; Tonina & Buffington, 2007) and sinuosity of river (Boano et al., 2006; Cardenas, 2009) on hyporheic exchange. Recent field studies show that the

presence of vegetation in stream increases the in-stream transient storage controlled by hyporheic exchange (Ensign & Doyle, 2005; Salehin et al., 2003). However, the impact of in-channel aquatic vegetation on the hyporheic exchange has not been systematically quantified (Ding et al., 2020).

In-channel aquatic vegetation exerts drag on the surface flow (Cheng & Nguyen, 2011; D'Ippolito et al., 2019), which creates spatial heterogeneities in near-bed mean flow velocity (Zhao & Fan, 2019), shear stress (Salvador et al., 2007; Yang et al., 2015), turbulent kinetic energy (Xu & Nepf, 2020), and pressure (Nepf & Koch, 1999; Yuan et al., 2021). In addition, vegetation drag also extracts energy from the mean flow and converts it to turbulent kinetic energy k_t (Nepf, 1999, 2012; Tanino & Nepf, 2008). Both spatial heterogeneity in hydraulic head (Boano et al., 2014; Lee et al., 2022; Shen et al., 2020; Tonina & Buffington, 2007; Yuan et al., 2021) and turbulence (Roche et al., 2018; Roche et al., 2019; Rousseau & Ancey, 2020; Voermans et al., 2017; Voermans et al., 2018b) are known to induce hyporheic exchange. Therefore, we anticipate that the drag exerted by vegetation, which induces spatial hydraulic gradient and turbulence, can induce hyporheic exchange.

The goal of this study is to quantify the impact of emergent vegetation, i.e., plants that extend out of the water surface, on hyporheic exchange across the sediment-water interface in streams with a flat gravel bed through systematically controlled laboratory experiments. We conducted a series of dye-visualization experiments in a water-recirculating flume filled with transparent hydrogel beads that simulate a gravel bed and acrylic cylinders that simulate emergent vegetation stems. We used an effective hyporheic exchange velocity, V_H, to characterize the exchange rate of fluorescent dye between surface and subsurface water in the hyporheic zone. In addition, the mean flow velocities were measured and the near-bed turbulent kinetic energy k_t was calculated. Our experiments show that V_H in channels with emergent vegetation scales with k_t when $k_t < 6 \times 10^{-4}$ $\mathrm{m^2/s^2}$, because k_t reflects the vegetation-drag-induced near-bed turbulence and spatial heterogeneity in hydraulic head, both of which drive hyporheic exchange.

2 Theories

2.1 Pseudo-first-order equations for hyporheic exchange

Here, we use pseudo-first-order equations (Wu et al., 2001) to quantify the impacts of the vegetation on the rate of solute exchange across the sediment-water interface. We hypothesized that Fick's first law governs the vertical hyporheic flux in vegetated channels with gravel flat beds, like the gas diffusion across a diffusive boundary layer. Thus, similar to gas transfer model based on the thin-film theory (Jørgensen & Revsbech, 1985; O'Connor & Hondzo, 2008), the rate of hyporheic exchange can be quantified by an effective hyporheic exchange velocity V_H. Note that here we focus on the hyporheic exchange between the surface water and the top sediment layers. We do not consider the variation in diffusivity with depth within deeper sediment as discussed in Chandler et al. (2016) and the longitudinal dispersion discussed in Bottacin-Busolin (2017). Below we describe how we use V_H and the pseudo-first-order equations to predict the release of solutes from the pore water of the top sediment layers to the surface water in a recirculating flume. In Section 3, we describe how we use flume experiments to validate the model.

First, at the beginning of the experiment, a solute is uniformly distributed in the pore space of the top several layers of sediment with concentration C_s. Due to hyporheic exchange, the solute in the sediment is transported into the surface water through a mixing layer, such that C_s decreases with time t. Once solute leaves the sediment bed, it is quickly mixed with the surface water with

a uniform concentration C_w. For simplicity, we assume that the solute concentrations in the top sediment layers and in surface water are both uniformly distributed, with volume $V_{ol,s}$ and $V_{ol,w}$, respectively. We hypothesize that the exchange between surface and subsurface water at the sediment-water interface can be characterized by a pair of pseudo-first-order equations with an effective hyporheic exchange velocity V_H. Therefore, based on mass balance between the surface water and subsurface water:

$$\frac{dC_s}{dt} = -V_H \frac{A_{SWI}\phi_s}{V_{ol,s}}(C_s - C_w) \quad (1)$$

$$\frac{dC_w}{dt} = -V_H \frac{A_{SWI}\phi_s}{V_{ol,w}}(C_w - C_s). \quad (2)$$

Here ϕ_s is the sediment porosity; A_{SWI} is the horizontal area of the sediment-water interface (m^2), and V_H is the effective hyporheic exchange velocity ($\mathrm{m/s}$), which is defined as $V_H = D_e/\delta_D$. D_e is the effective diffusion coefficient (m^2/s) and δ_D is the mixing layer thickness (m). If the solute concentration in the surface water is negligible ($C_s \gg C_w$), the analytical solution of Eq. 1 is $C_s(t) = C_{s0}e^{-V_H A_{SWI}\phi_s t/V_{ol,s}}$, which predicts an exponential decrease in the solute concentration in the pore space of the sediment. Here C_{s0} indicates the initial solute concentration in the sediment. The schematic diagram of the proposed model is shown in Fig. S1 in the Supplementary Information. The fitting of this model (Eqs. 1 and 2) to our experimental results are discussed in Section 4.1. Note that effective diffusion coefficient D_e was defined differently using 1-D diffusion equation in other studies (Chandler et al., 2016; Grant et al., 2012; O'Connor & Harvey, 2008). Comparisons of the D_e based on their definition is discussed in Section 4.1.

2.2 Impact of emergent vegetation on hyporheic exchange

In-channel vegetation exerts drag on surface flow (Cheng & Nguyen, 2011; D'Ippolito et al., 2019) and converts kinetic energy of the mean flow to turbulent kinetic energy (Nepf, 1999; Tanino & Nepf, 2008). The drag force generated by vegetation can be expressed as follows (Cheng & Nguyen, 2011),

$$F_D = \frac{1}{2} a V_{ol,v} C_D \rho_w U^2 \quad (3)$$

Here a is the frontal area per unit volume (m^{-1}) which can be estimated as $a = nd_v$ for cylindrical vegetation (Yang & Nepf, 2018); n is the stem density ($\mathrm{stem/m}^2$); d_v is the diameter of model vegetation stem (m); C_D is the drag coefficient of the vegetation; $V_{ol,v}$ is the volume of water with vegetation canopy (m^3); ρ_w is fluid density ($\mathrm{kg/m}^3$), and U is the flow velocity ($\mathrm{m/s}$). The drag exerted by the emergent vegetation generates spatial heterogeneities in the near-bed mean flow velocity, and further generated the hydraulic head that induces the hyporheic exchange (Yuan et al., 2021). In addition, the vegetation-generated turbulent kinetic energy k_{tv} can be estimated by the energy extracted from the mean flow due to vegetation drag (Tanino & Nepf, 2008; Yang et al., 2016):

$$k_{tv} = 1.2\left[C_D \frac{\phi_v}{(1-\phi_v)\,\pi/2}\right]^{2/3} U^2. \quad (4)$$

Here ϕ_v is the solid fraction of the vegetation. For cylindrical dowels, $\phi_v = \pi a d_v/4$ (Yang & Nepf, 2018). The total near-bed turbulent kinetic energy k_t then can be approximated as the sum of bed-generated k_{tb} and vegetation-generated k_{tv} (Yang et al., 2016; Yang & Nepf, 2018, 2019),

$$k_t = k_{tb} + k_{tv}. \quad (5)$$

Here $k_{tb} = C_f U^2/0.19$; C_f is bed drag coefficient. The vegetation generated turbulence is a result of vegetation drag and as thus correlates with the spatial heterogeneity in hydraulic head which is also induced by vegetation drag. We hypothesis that near-bed turbulent kinetic energy k_t reflects the compound effect of vegetation-drag-induced spatial heterogeneity in near-bed hydraulic head and near-bed turbulence on hyporheic exchange and thus k_t can be applied to predict the vegetation-induced hyporheic exchange.

3 Materials and Methods

3.1 Experimental setup

Hyporheic exchange experiments were conducted in a horizontal race-track flume at the University of Minnesota's St. Anthony Falls Laboratory. The flume is 14-m-long and 60-cm-wide and has a 150-cm-long by 60-cm-wide straight test section (Figs. 1 and S2). The water depth in all experiments was 20.0 ± 0.1 cm. The flow in the flume was driven by a propeller. The flow velocity was directly measured by a side-looking Acoustic Doppler Velocimeter (Nortek Vectrino, Norway, Fig. S5).

The bottom of the test section (60 cm × 150 cm) was removed, and the space underneath was filled with transparent hydrogel beads (5.6 ± 0.6 mm in diameter) to simulate a gravel bed. Method to make the hydrogel beads developed by Ma et al. (2019) is described in Text S1 in the Supplementary Information. To keep the hydrogel beads in place and the sediment bed flat, a black polyester mesh (4 mm pore size) was placed on the top of the beads. While the bed was mostly flat without obvious bedform, one of the downstream corners of the mesh tilted and formed a small lateral slop of 1/150 and 1/60 in streamwise direction and spanwise direction, respectively. This structure was roughly the same in both cases with and without vegetation. We anticipate this small structure would not affect our results, because we focus on the difference in hyporheic exchange between channels with and without vegetation.

To investigate the impact of rigid emergent vegetation on the flow, the translucent and cylindrical acrylic dowels with $d_v = 6.4 \pm 0.1$ mm diameter were inserted in a staggered pattern (Fig. S5) on a PVC board fixed under the sediments. The dowels extended through the whole water column and entire sediment depth. The solid volume fraction of vegetation ϕ_v in this study is 0.05, in the range of typical values found in marshes (Nepf, 2012; Yang et al., 2016). The stem density n is 1,514 $\mathrm{stems/m^2}$, and the spanwise center-to-center distance between two dowels $2ds$ is 2.6 cm (Fig. S5). The vegetation frontal area per unit canopy volume $a = nd$ is 9.8 $\mathrm{m^{-1}}$. There are 1,363 dowls in the test section. In the area where images were processed, there were 47 dowels.

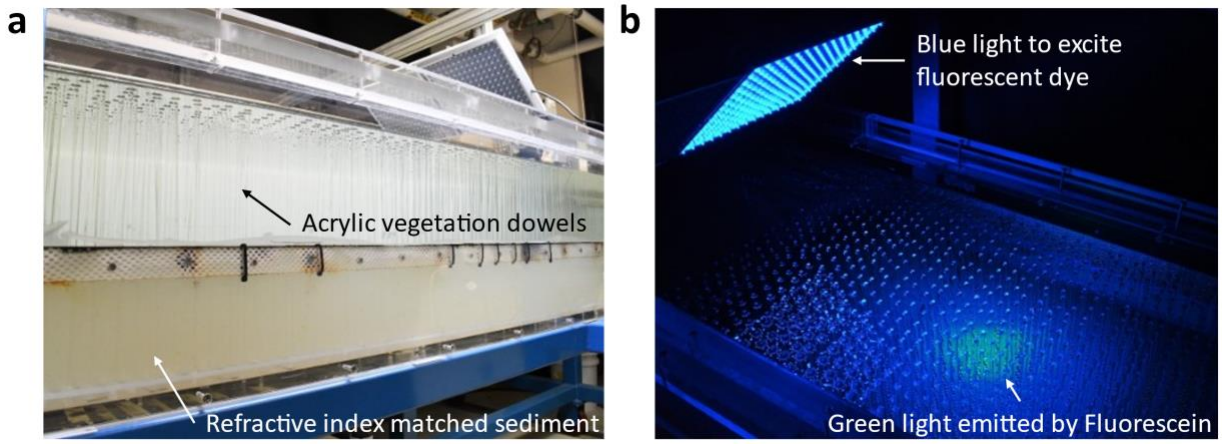

Figure 1. Experiments in a recirculating flume to visualize the exchange of fluorescent dye between surface and subsurface water. Refractive-index-matched sediment and translucent vegetation dowels were used. Green, fluorescent dye was injected into the sediment and a blue lamp was used to excite the dye.

Instantaneous flow velocity was measured using a side-looking Acoustic Doppler Velocimeter (ADV; Nortek Vectrino, Norway) mounted on a 2-D moving system with 200 Hz sampling rate for 2.5 minutes. Solid glass beads with specific gravity 2.6 and mean diameter 35 micrometers (3000 E-Spheriglass; Potters Industries Inc., Pennsylvania) were added to the water as seeding particles. Measurements with signal-to-noise ratio below 15 dB were removed from data analysis. A bivariate kernel density function was used to remove noise signals from velocity measurements (Islam & Zhu, 2013). For cases with vegetation, three dowels were removed to make space for the probe of the ADV. We anticipate that the ADV probe would not affect the velocity measurements, because the probe was 5 cm away from the measurement location (Fig. S5). Four velocity profiles were measured at the middle of test section to estimate spatial-weighted averaged velocities for each case. For cases without vegetation, profiles were 5, 13, 22, 30 cm away from the side wall, respectively. The measured locations and weighted average method for cases with vegetation can be found in Fig. S5.

The spatially averaged near-bed turbulent kinetic energy k_t was calculated from the instantaneous flow velocity measured 2 cm above the bed at the four representative locations using an ADV. Specifically, the local k_t at each location was calculated as $\left(\overline{u'^2} + \overline{v'^2} + \overline{w'^2}\right)/2$. Here u', v', and w' are flow velocity fluctuations in streamwise, spanwise, and vertical direction, respectively. The spatially averaged near-bed k_t was calculated using a spatial-average method justified in Yang et al. (2015) from local k_t at 4 locations as shown in Fig. S5. Location at 2 cm above bed was chosen because within 2 cm from the bed the sampling volume of the ADV is interfered by the boundary such that the signal-to-noise ratio became smaller than 15 dB. Previous studies using same model vegetation show that the vertical distribution of turbulent kinetic energy is uniform above a thin boundary layer (Nepf, 1999; Yang et al., 2015), thus, our measurement of k_t at 2 cm above the bed captures the impacts of vegetation on near-bed turbulent kinetic energy.

198 3.2 Fluorescent dye release experiments

199 Fluorescent dye release experiments were conducted to measure the rate of hyporheic
200 exchange. First, dye solution was prepared by adding fluorescein sodium salt (Sigma-Aldrich
201 F6377) to DI water at 0.002‰ weight ratio. The water depth in the flume was adjusted to 20.0 ±
202 0.1 cm. The fluorescent dye was injected into a 44 cm × 43 cm sediment area up to 5 cm deep
203 (accumulative dye concentration is $(1.286 \pm 0.006) \times 10^{-3}$ mg/cm^2) using a peristaltic pump (L/S
204 7550-50; Masterflex, Germany). The flow was stopped during the injection. The amount of dye
205 injected at each location was monitored by a scale during the injection process to make sure the
206 uniformly distribution of dye within the injection area. The dye emits green light at 520-nm
207 wavelength, when it is excited by blue light at 490-nm wavelength (Osenbroch et al., 2005). The
208 fluorescence intensity detected by downward-looking camera were calibrated against the dye
209 concentration in the sediment (Text S2 and Fig. S6 in the Supplementary Information). Our
210 measurements indicate that the fluorescence intensity is linearly proportional to the accumulative
211 dye concentration, i.e., mass per unit area (Fig. S6a). The picture of injection equipment and
212 injection locations can be found in Figs. S7-S8.

213 One square lamp (30 cm × 30 cm) with blue LED arrays were placed at the center of the
214 channel and 33 cm above the water surface. The angle between lamp and ground was 40°. The
215 light emitted from the dye was passed through a green light filter (FGV9S; Thorlabs, Newton) and
216 captured by a downward-looking industrial camera (BFS-U3-16S2C-CS; FLIR Systems,
217 Wilsonville) with a 6 mm focal length lens (ArduCAM, China) placed 120 cm above the sediment
218 bed. Afterwards, flow was recirculated in the flume using a propeller, and the fluorescence
219 intensity within the sediment bed was monitored every 5 minutes for a 16.6-hour duration. The
220 unsteady period of flow development at the beginning of the experiment is relatively short (few
221 minutes) compared to the time scale of whole experiment (> 16.6 hours) and the data at early stage
222 was not included in the model fits (Text S3 in the Supplementary Information). Experiments
223 without vegetation were conducted at mean flow velocities of 1.7, 4.0, 6.6, 15.4 cm/s. Experiments
224 with vegetation were conducted at flow velocities of 0.7, 1.6, 2.4, 3.6 cm/s. Each case was
225 conducted twice.

226 The effective hyporheic exchange velocity V_H was estimated by fitting the numerical
227 solution of the pseudo-first-order equation (Eq. 1) to the measured fluorescence intensity versus
228 time (Fig. 2). First, pixels occupied by vegetation and the mesh were removed, and the
229 fluorescence intensity of the light emitted by the dye in the sediment was estimated by averaging
230 the image intensity of pixels occupied by the pore space. From the series of images, the curve of
231 fluorescence intensity versus time, i.e., washout curve, can be obtained. Then, the proposed model
232 (Eqs. 1-2) were fitted numerically to the measured fluorescence intensity versus time (Fig. 2). The
233 effective hyporheic exchange velocity V_H and background image intensity was determined by
234 minimizing the root mean square error between the measured curve and the simulated curve. The
235 detail image processing method and fitting procedure can be found in Text S3 and Fig. S10 in the
236 Supplementary Information.

237 To compare the effective hyporheic exchange velocities V_H for the cases without and with
238 vegetation, we conducted the one-way analysis of covariance (ANOCOVA) using 'aoctool'
239 function in MATLAB, with p-value indicating the statistical difference (Philippas, 2014). When
240 $p < 0.05$, the difference between two data sets is often considered to be statistically significant.

Note that once dye leaves the sediment, it is quickly diluted in the surface water. Our experiments show that the dye in the surface water, whose concentration is much smaller than the dye concentration in the sediment, does not affect the results, i.e., the light captured by the camera above the water surface is mainly contributed by the dye in the sediment.

4 Results

4.1 Dye release experiments verify the proposed model

First, we use dye release experiments described in Section 3.2 to verify the proposed hyporheic exchange model (Eqs. 1-2). The fluorescence intensity at different times shows that the dye concentration in the sediment bed decreases over time (Fig. S9). The spatially averaged fluorescence intensity of the green light emitted by the fluorescent dye was plotted versus time to characterize the leaving of dye from the observed area. The method to identify the pixels related to the pore space can be found in Text S3 in the Supplementary Information. Fig. 2 shows two representative cases without and with vegetation at a similar spatially and temporally averaged flow velocity U measured by an ADV. The decrease in dye concentration occurred much faster in a channel with vegetation than in a channel without vegetation, indicating that the presence of vegetation increases the hyporheic exchange rate.

To capture the rate of exchange, we fit the spatially averaged fluorescence intensity versus time measurements with the proposed model (Eqs. 1 and 2) numerically (see Text S3 in the Supplementary Information for details). The fitted results (solid curves in Fig. 2) show an exponential decrease in fluorescence intensity. The predictions of the model are consistent with the data which were not included in the fitting of the effective hyporheic exchange velocity V_H (dash lines in Fig. 2), indicating that the proposed model can be used to characterize the hyporheic exchange observed in the experiments.

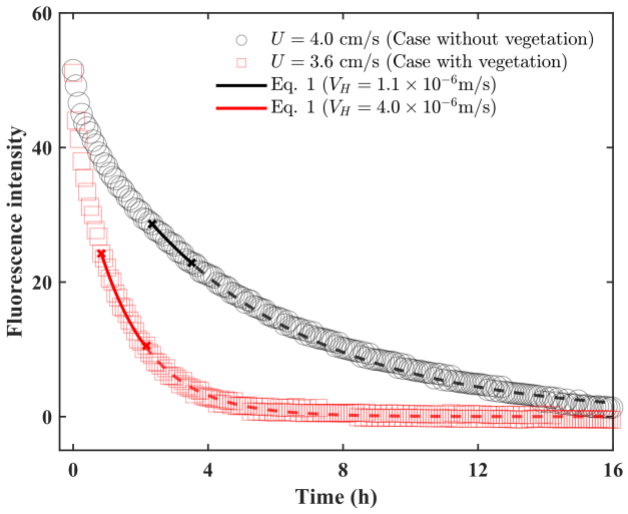

Figure 2. The concentration of the fluorescent dye in the sediment, represented by the fluorescence intensity of the emitted green light, decays over time. The flow was started at time = 0 hour. The black and red symbols represent the fluorescence intensities relative to the background image intensities in channels without vegetation and with vegetation of volume fraction $\phi_v = 0.05$, respectively, at a similar flow velocity 4 cm/s. The black and red solid curves represent the fits of

the measurements with the solution of Eq. 1 with both $R^2 = 0.99$. The model fits are conducted when the streamwise fluorescence intensity decrease uniformly (see Text S3 in the Supplementary Information for details). In the experiments, the horizontal area of the sediment-water interface $A_{SWI} = 0.19\ \mathrm{m}^2$; the sediment porosity $\phi_s = 0.3$; the volume of pore space in the sediment $V_{ol,s} = 1200 \pm 9$ mL, and the volume of surface water $V_{ol,w} = 2830$ L. The fitted parameters are V_H and background image intensity. Dash lines show the model predictions.

Note that in the complementary dye release experiments with a side-looking camera, we observed a streamwise elongation of dye plume. The velocity of the dye front is 1.0~1.5% of the velocity of overlying flow to the downstream in the sediment, which is not considered in the proposed model. On the other hand, the vertical mixing of dye in the sediment was not significant compared with the exchange of dye at the sediment-water interface (Text S4 in the Supplementary Information).

At a similar flow velocity around 4 cm/s, the effective hyporheic exchange velocity V_H of the case without vegetation is 1.1×10^{-6} m/s, about 4 times smaller than V_H of the case with vegetation which $V_H = 4.0 \times 10^{-6}\ \mathrm{m/s}$ (Fig. 2). In addition, the slope of regression line of cases with vegetation is 4 times higher than the slope of regression line of cases without vegetation (Fig. 3a). These results indicate that the presence of vegetation increases the rate of hyporheic exchange by a factor of 4 at the same mean flow velocity U.

Finally, we provide comparison of our results with pervious study. The effective diffusion coefficients D_e calculated using 1-D diffusion equation in our experiments are provided in Table S1 and are compared with the interfacial transport model proposed by Volermans et al. (2018a) in Fig. S12 in the Supplementary Information.

4.2 The scale of effective hyporheic exchange velocity with turbulent kinetic energy

By comparing V_H versus U and k_t for cases without and with vegetation, we exam whether the exchange rate at the sediment-water interface is controlled by mean flow velocity or turbulent kinetic energy. Based on ANOCOVA (see methods for details), the difference between lines V_H versus U measurements for cases without and with vegetation is statistically significant (with $p = 0$ smaller than statistical threshold value 0.05). In contrast, at $k_t < 6 \times 10^{-4}\ \mathrm{m^2/s^2}$, the difference between the slopes of lines V_H versus k_t measurements for cases without and with vegetation is not significant ($p = 0.26$; Fig. 3b). Note that the intercept of line V_H versus k_t without vegetation is statistically significantly bigger than the intercept of line with vegetation and V_H in the vegetated case with $k_t = 7.4 \times 10^{-4}\ \mathrm{m^2/s^2}$ deviates from the linear fitting for $k_t < 6 \times 10^{-4}\ \mathrm{m^2/s^2}$. These deviations are reflections of the complex interactions of flow and vegetation, especially at high turbulent conditions. Nevertheless, our results show that compared with mean flow velocity, turbulent kinetic energy is a better predictor of hyporheic exchange for channels with vegetation, especially at $k_t < 6 \times 10^{-4}\ \mathrm{m^2/s^2}$.

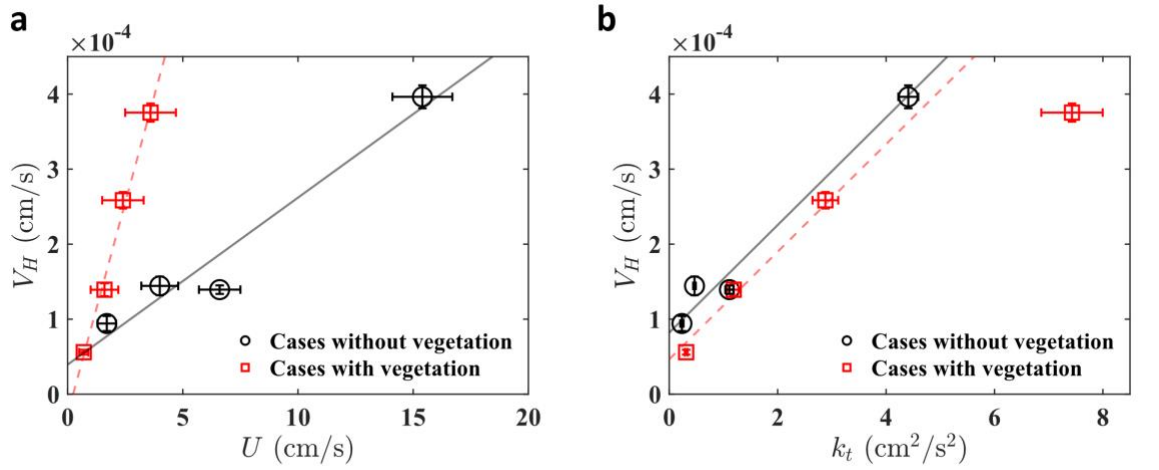

Figure 3. (a) The effective hyporheic exchange velocity V_H versus mean flow velocity U of cases without vegetation (black) and with vegetation of volume fraction $\phi_v = 0.05$ (red). The black solid line ($y = (0.2x + 0.4) \times 10^{-4}$) and red dash line ($y = (1.1x - 0.3) \times 10^{-4}$) represent linear fits to measurements without and with vegetation with $R^2 = 0.89$ and $R^2 = 0.95$, respectively. (b) V_H versus the total near-bed turbulent kinetic energy k_t of cases without vegetation (black) and with vegetation (red). The black solid line ($y = (7.2x + 8.2) \times 10^{-5}$) and red dash line ($y = (7.2x + 4.7) \times 10^{-5}$) represent linear fits of the measurements without and with vegetation with both $R^2 = 0.92$.

5 Conclusions

Vegetation has been acknowledged to enhance the exchange between surface and subsurface water in the aquatic habitats, yet the impacts of vegetation on hyporheic exchange have not been characterized. Here we propose a model to characterize the vegetation-induced hyporheic exchange in channels with vegetation. By conducting tracer experiments using fluorescent dye and refractive-index-matched sediment, we show that the vegetation-induced hyporheic exchange at the sediment-water interface can be characterized by the pseudo-first-order equations with an effective hyporheic exchange velocity V_H. We demonstrate that at the same spatially and temporally averaged flow velocity U, vegetation increases V_H by up to a factor of four when compared with channels without vegetation. We further demonstrate that V_H scales with the total near-bed turbulent kinetic energy k_t instead of U when $k_t < 6 \times 10^{-4}$ m^2/s^2. The results of the proposed hyporheic exchange model will enable quantitative analysis of the impacts of vegetation on the exchange of contaminants and nutrients in the hyporheic zone.

Acknowledgments

This study was supported by JQ Yang's startup funds and Minnesota Water Research Fund. The authors would like to thank Sam Nguyen for his assistance with the experiments, Peter Kang for insightful discussions, and Benjamin Erickson, Erik Steen, and Jeffrey Marr for help with the flume.

Data Availability Statement

The raw data of the dye release experiments with a downward-looking camera has been deposited in The Data Repository for University of Minnesota (https://doi.org/10.13020/W282-JJ11). The raw data of the dye release experiments with a side-looking camera and dye calibration have been deposited on Zenodo (https://doi.org/10.5281/zenodo.6412364).

The codes used to process the images and fit the washout curves have been deposited on Zenodo (https://doi.org/10.5281/zenodo.6407198).

References

Battin, T. J., Kaplan, L. A., Findlay, S., Hopkinson, C. S., Marti, E., Packman, A. I., . . . Sabater, F. (2008). Biophysical controls on organic carbon fluxes in fluvial networks. *Nature geoscience*, *1*(2), 95-100.

Boano, F., Camporeale, C., Revelli, R., & Ridolfi, L. (2006). Sinuosity-driven hyporheic exchange in meandering rivers. *Geophysical Research Letters*, *33*(18).

Boano, F., Harvey, J. W., Marion, A., Packman, A. I., Revelli, R., Ridolfi, L., & Wörman, A. (2014). Hyporheic flow and transport processes: Mechanisms, models, and biogeochemical implications. *Reviews of Geophysics*, *52*(4), 603-679.

Bottacin-Busolin, A. (2017). Non-Fickian dispersion in open-channel flow over a porous bed. *Water Resources Research*, *53*(8), 7426-7456.

Boulton, A. J., Findlay, S., Marmonier, P., Stanley, E. H., & Valett, H. M. (1998). The functional significance of the hyporheic zone in streams and rivers. *Annual review of Ecology and systematics*, *29*(1), 59-81.

Buffington, J. M., & Tonina, D. (2009). Hyporheic exchange in mountain rivers II: Effects of channel morphology on mechanics, scales, and rates of exchange. *Geography Compass*, *3*(3), 1038-1062.

Cardenas, M. B. (2009). A model for lateral hyporheic flow based on valley slope and channel sinuosity. *Water Resources Research*, *45*(1).

Chandler, I., Guymer, I., Pearson, J., & Van Egmond, R. (2016). Vertical variation of mixing within porous sediment beds below turbulent flows. *Water resources research*, *52*(5), 3493-3509.

Cheng, N.-S., & Nguyen, H. T. (2011). Hydraulic radius for evaluating resistance induced by simulated emergent vegetation in open-channel flows. *Journal of hydraulic engineering*, *137*(9), 995-1004.

Ding, M., Wan, J., Li, Q., & Tang, B. (2020). Literature Review: How in-channel aquatic vegetation (IAV) affects hyporheic exchange (HE). IOP Conference Series: Materials Science and Engineering,

Dudunake, T., Tonina, D., Reeder, W., & Monsalve, A. (2020). Local and Reach-Scale Hyporheic Flow Response From Boulder-Induced Geomorphic Changes. *Water Resources Research*, *56*(10), e2020WR027719.

D'Ippolito, A., Lauria, A., Alfonsi, G., & Calomino, F. (2019). Investigation of flow resistance exerted by rigid emergent vegetation in open channel. *Acta Geophysica*, *67*(3), 971-986.

Ensign, S. H., & Doyle, M. W. (2005). In-channel transient storage and associated nutrient retention: Evidence from experimental manipulations. *Limnology and oceanography*, *50*(6), 1740-1751.

Gooseff, M. N. (2010). Defining hyporheic zones–advancing our conceptual and operational definitions of where stream water and groundwater meet. *Geography Compass*, *4*(8), 945-955.

Grant, S. B., Stewardson, M. J., & Marusic, I. (2012). Effective diffusivity and mass flux across the sediment-water interface in streams. *Water Resources Research*, *48*(5).

Grant, S. B., Stolzenbach, K., Azizian, M., Stewardson, M. J., Boano, F., & Bardini, L. (2014). First-order contaminant removal in the hyporheic zone of streams: Physical insights from a simple analytical model. *Environmental science & technology*, *48*(19), 11369-11378.

Huang, S.-H., & Yang, J. Q. (2021). *Experimental data of vegetation-induced hyporheic exchange experiment in Ecoflume of St. Anthony Falls Laboratory on 2021 (29GB)*. https://doi.org/10.13020/W282-JJ11

Huang, S.-H., & Yang, J. Q. (2022a). *Data of complementary experiments of 'Vegetation-induced hyporheic exchange experiment in Ecoflume of St. Anthony Falls Laboratory on 2021'* Version 1.0.0). https://doi.org/10.5281/zenodo.6412364

Huang, S.-H., & Yang, J. Q. (2022b). *Shih-HsunHuang/Vegetated-induced-hyporheic-exchange* Version v1.1.0). https://doi.org/10.5281/zenodo.6407198

Islam, M. R., & Zhu, D. Z. (2013). Kernel density–based algorithm for despiking ADV data. *Journal of Hydraulic Engineering*, *139*(7), 785-793.

Jones Jr, J. B., & Holmes, R. M. (1996). Surface-subsurface interactions in stream ecosystems. *Trends in Ecology & Evolution*, *11*(6), 239-242.

Jørgensen, B. B., & Revsbech, N. P. (1985). Diffusive boundary layers and the oxygen uptake of sediments and detritus 1. *Limnology and oceanography*, *30*(1), 111-122.

Lee, A., Aubeneau, A. F., Cardenas, M. B., & Liu, X. (2022). Hyporheic exchange due to cobbles on sandy beds. *Water Resources Research*, e2021WR030164.

Lewandowski, J., Putschew, A., Schwesig, D., Neumann, C., & Radke, M. (2011). Fate of organic micropollutants in the hyporheic zone of a eutrophic lowland stream: Results of a preliminary field study. *Science of the Total Environment*, *409*(10), 1824-1835.

Ma, L., Shi, Y., Siemianowski, O., Yuan, B., Egner, T. K., Mirnezami, S. V., . . . Cademartiri, L. (2019). Hydrogel-based transparent soils for root phenotyping in vivo. *Proceedings of the National Academy of Sciences*, *116*(22), 11063-11068.

Marion, A., Bellinello, M., Guymer, I., & Packman, A. (2002). Effect of bed form geometry on the penetration of nonreactive solutes into a streambed. *Water Resources Research*, *38*(10), 27-21-27-12.

McCallum, J. L., Höhne, A., Schaper, J. L., Shanafield, M., Banks, E. W., Posselt, M., . . . Lewandowski, J. (2020). A numerical stream transport modeling approach including multiple conceptualizations of hyporheic exchange and spatial variability to assess contaminant removal. *Water Resources Research*, *56*(3), e2019WR024987.

Nepf, H. M. (1999). Drag, turbulence, and diffusion in flow through emergent vegetation. *Water resources research*, *35*(2), 479-489.

Nepf, H. M. (2012). Flow and transport in regions with aquatic vegetation. *Annual review of fluid mechanics*, *44*, 123-142.

Nepf, H. M., & Koch, E. W. K. (1999). Vertical secondary flows in submersed plant-like arrays. *Limnology and oceanography*, *44*(4), 1072-1080.

O'Connor, B. L., & Harvey, J. W. (2008). Scaling hyporheic exchange and its influence on biogeochemical reactions in aquatic ecosystems. *Water Resources Research*, *44*(12).

O'Connor, B. L., & Hondzo, M. (2008). Dissolved oxygen transfer to sediments by sweep and eject motions in aquatic environments. *Limnology and Oceanography*, *53*(2), 566-578.

Osenbroch, L. K. H., Hjertager, B. H., & Solberg, T. (2005). Experiments and CFD modelling of fast chemical reaction in turbulent liquid flows. *International Journal of Chemical Reactor Engineering*, *3*(1).

Packman, A. I., Salehin, M., & Zaramella, M. (2004). Hyporheic exchange with gravel beds: Basic hydrodynamic interactions and bedform-induced advective flows. *Journal of Hydraulic Engineering*, *130*(7), 647-656.

Philippas, D. (2014). Analysis of Covariance (ANCOVA). In A. C. Michalos (Ed.), *Encyclopedia of Quality of Life and Well-Being Research* (pp. 157-161). Springer Netherlands. https://doi.org/10.1007/978-94-007-0753-5_82

Roche, K., Blois, G., Best, J., Christensen, K., Aubeneau, A., & Packman, A. (2018). Turbulence links momentum and solute exchange in coarse-grained streambeds. *Water Resources Research*, *54*(5), 3225-3242.

Roche, K. R., Li, A., Bolster, D., Wagner, G. J., & Packman, A. I. (2019). Effects of turbulent hyporheic mixing on reach-scale transport. *Water Resources Research*, *55*(5), 3780-3795.

Rousseau, G., & Ancey, C. (2020). Scanning PIV of turbulent flows over and through rough porous beds using refractive index matching. *Experiments in Fluids*, *61*(8), 1-24.

Salehin, M., Packman, A. I., & Wörman, A. (2003). Comparison of transient storage in vegetated and unvegetated reaches of a small agricultural stream in Sweden: seasonal variation and anthropogenic manipulation. *Advances in Water Resources*, *26*(9), 951-964.

Salvador, G. P., Stoesser, T., Rummel, A. C., & Rodi, W. (2007). Turbulent shallow flow through vegetation. Fifth International Symposium on Environmental Hydraulics (ISEH V),

Shen, G., Yuan, J., & Phanikumar, M. S. (2020). Direct numerical simulations of turbulence and hyporheic mixing near sediment–water interfaces. *Journal of Fluid Mechanics*, *892*.

Tanino, Y., & Nepf, H. M. (2008). Lateral dispersion in random cylinder arrays at high Reynolds number. *Journal of Fluid Mechanics*, *600*, 339-371.

Tonina, D., & Buffington, J. M. (2007). Hyporheic exchange in gravel bed rivers with pool-riffle morphology: Laboratory experiments and three-dimensional modeling. *Water Resources Research*, *43*(1).

Tonina, D., & Buffington, J. M. (2009). Hyporheic exchange in mountain rivers I: Mechanics and environmental effects. *Geography Compass*, *3*(3), 1063-1086.

Voermans, J., Ghisalberti, M., & Ivey, G. (2017). The variation of flow and turbulence across the sediment–water interface. *Journal of Fluid Mechanics*, *824*, 413-437.

Voermans, J. J., Ghisalberti, M., & Ivey, G. N. (2018a). A model for mass transport across the sediment-water interface. *Water Resources Research*, *54*(4), 2799-2812.

Voermans, J. J., Ghisalberti, M., & Ivey, G. N. (2018b). The Hydrodynamic Response of the Sediment-Water Interface to Coherent Turbulent Motions. *Geophysical Research Letters*, *45*(19), 10,520-510,527.

Wohl, E. (2016). Spatial heterogeneity as a component of river geomorphic complexity. *Progress in Physical Geography*, *40*(4), 598-615.

Wu, F.-C., Tseng, R.-L., & Juang, R.-S. (2001). Kinetic modeling of liquid-phase adsorption of reactive dyes and metal ions on chitosan. *Water research*, *35*(3), 613-618.

Xu, Y., & Nepf, H. (2020). Measured and predicted turbulent kinetic energy in flow through emergent vegetation with real plant morphology. *Water Resources Research*, *56*(12), e2020WR027892.

Yang, J. Q., Chung, H., & Nepf, H. M. (2016). The onset of sediment transport in vegetated channels predicted by turbulent kinetic energy. *Geophysical Research Letters*, *43*(21), 11,261-211,268.

Yang, J. Q., Kerger, F., & Nepf, H. M. (2015). Estimation of the bed shear stress in vegetated and bare channels with smooth beds. *Water Resources Research*, *51*(5), 3647-3663.

Yang, J. Q., & Nepf, H. M. (2018). A turbulence-based bed-load transport model for bare and vegetated channels. *Geophysical Research Letters*, *45*(19), 10,428-410,436.

Yang, J. Q., & Nepf, H. M. (2019). Impact of vegetation on bed load transport rate and bedform characteristics. *Water Resources Research*, *55*(7), 6109-6124.

Yuan, Y., Chen, X., Cardenas, M. B., Liu, X., & Chen, L. (2021). Hyporheic exchange driven by submerged rigid vegetation: a modeling study. *Water Resources Research*, *57*(6), e2019WR026675.

Zhao, M.-d., & Fan, Z.-l. (2019). Emergent vegetation flow with varying vertical porosity. *Journal of Hydrodynamics*, *31*(5), 1043-1051.

Geophysical Research Letters

Supporting Information for

Impacts of Emergent Vegetation on Hyporheic Exchange

S. Huang[1,2], and J. Q. Yang[1,2]

[1] Saint Anthony Falls Laboratory, University of Minnesota, Minneapolis, MN 55414.

[2] Department of Civil, Environmental, and Geo-Engineering, University of Minnesota, Minneapolis, MN 55455.

Contents of this file

Introduction

This supporting information contains Text S1-S4, Figs. S1-S12, and Table S1. In Text S1, the procedure to make hydrogel beads used in the experiments is briefly summarized. Text S2 provides details of dye calibration. Image processing steps that were used to calculate the washout curves and the fitting process of the proposed model are described in Text S3. Text S4 discusses the results of experiment with a side-looking camera.

Fig. S1 is the schematic diagram of the proposed model.
Fig. S2 shows the diagram of the flume.
Figs. S3 and S4 are images show the process to make hydrogel beads.
Fig. S5 shows the location of velocity measurements of the cases with vegetation.
Fig. S6 shows the results of dye calibration.
Figs. S7 and S8 show the injection equipment and dye injection locations.
Fig. S9 shows the snapshots of the sediment bed at different times.
Fig. S10 describes the imaging processing steps.
Fig. S11 shows the results of the experiments with a side-looking camera.
Fig. S12 compares the effective diffusion coefficients of cases without vegetation with the previous study.
Table S1 lists the flow conditions of each case.

Text S1.

The hydrogel beads were made following the procedure proposed by Ma et al. (2019). First, sodium alginate (Sigma-Aldrich W201502) and gellan gum (Sigma-Aldrich P8169) were mixed with deionized water, and their final concentrations were 0.24 wt% and 0.96 wt%, respectively. To make sodium alginate and Gellan Gum fully dissolve into the water, the gel solution was autoclaved with the liquids cycle (sterilization temperature: 121 ℃, sterilize time: 30 minutes). After cooling down at least 12 hours, the polymer solution was dropped into 10 mM magnesium chloride solution ($MgCl_2$, Millipore 442611-M) through plastic tubes (4 mm I.D.), as shown in Fig. S3. The magnesium ions cause sodium alginate and gellan gum to cross link and form discrete spherical hydrogel beads (Fig. S4). The diameters of the hydrogel beads are 5.6±0.6 mm.

Text S2.

Two calibration tests were performed to confirm the linear relationship between the dye concentration in the sediment and the fluorescence intensity detected by the downward-looking camera. First, we placed an 8-cm-square box filled with beads and known concentrations of fluorescent dye under the mesh in flume filled with water. We illuminated the dye and hydrogel beads in the box with the blue LED lamp and measured the averaged fluorescence intensity of the emitted green light using the downward-looking camera with a green light filter. Because the beads are transparent, the image intensity detected by the downward looking camera represents the accumulative signal of fluorescence emitted by the dye at different depth. The results are shown in Fig. S6a. Our measurements show that the fluorescence intensity is linearly proportional to the accumulative dye concentration, or mass of dye per unit area, and the thickness of the beads does not affect the detected fluorescence intensities.

Second, we inject 5 mL of dye with concentration of 0.5, 1.0, 1.5 or 2.0×10^{-4} wt% into the sediment up to 5 cm deep at the same location within 10 seconds for all cases. The image of the sediment bed was taken by a downward-looking camera. A binary image mask was used to block the image outside the dye plume, and the pixels on the dye plume was identified by the procedure mentioned in Text S3. Finally, the florescence intensity detected by a downward-looking camera are calculated by averaging the image intensity of pixels on the dye plume. The results show that the relationship between fluorescence intensity and injected dye concentration is linear (Fig. S6b), suggesting that the fluorescence intensity is linearly related with dye concentration in the sediment. Note that because the dye was injected at the same location with similar flow rate (~0.5 mL/s), the dye plume volume and location of dye plume in the sediment is similar between cases, and dilute effect caused by transparent sediment is similar in the calibration tests. The injected volume 5 mL is the same with the volume of the dye injected in the dye release experiments at one location and 2.0×10^{-4} wt% is the initial concentration used in the experiments.

Text S3.

Here we describe the imaging processing steps to calculate the fluorescence intensity in the sediment from images shown in Fig. S9. First, the recorded images were cropped to an area contain several repeated patterns of vegetation dowels, and the area occupied by and near the vegetation dowels was removed. Second, the normalized histogram of intensity of remaining pixels was fitted by the sum of the probability density functions of two normal distributions (Fig. S10c). Based on the histograms, the pixels were classified into two categories: (i) pixels occupied by the mesh were identified as the pixels with intensity histogram following the distribution with lower mean intensity and (ii) pixels occupied by hydrogel beads and pore water were identified by pixels with intensity histogram following the distribution with higher mean intensity. Note that for consistency, the number of pixels belong to the two histograms were kept at 60:40 ratio.

To estimate the spatial variation of the hyporheic exchange, the analyzed area was further divided into four subregions. In each subregion, fluorescence intensity of the sediment was estimated by averaging the image intensity of pixels occupied by the hydrogel beads and pore water. From the series of images, four washout curves were obtained in each test. Two of the examples are shown in Fig. 2.

After we obtained the curves of fluorescence intensity versus time, we fitted the curves with the solution of the first order equation (Eq. 1). The background image intensity and the effective hyporheic exchange velocity V_H were chosen as fitting parameters. The fitting procedure includes two steps. First, we determined the duration when the streamwise fluorescence intensity decreases uniformly. The fluorescence intensity of original analyzed region was averaged in spanwise direction. Then, the resulting streamwise profiles were normalized by the profile at different times. If the slope of the normalized profile was not statistically different from zero, the normalized profile was horizontal, indicating that the fluorescence intensity decreases uniformly in streamwise direction (Fig. S11d). We fitted the model to the data during this time because the decrease in fluorescence intensity was mainly contributed by the leaving of dye from the sediment (Text S4). Secondly, the first order equations were solved numerically, and the fitting parameters were determined by minimizing the root mean square error between the simulated curve and measured curve from each subregion. Here the root mean square error was calculated by subtracting the linearly interpolated values of the simulated curve at the time when the images were taken. The background image intensity was first determined by fitting the whole washout curve with the solution of Eq. 1. Then, the effective hyporheic exchange velocity V_H were determined by fitting the measured fluorescence intensity when the streamwise fluorescence intensity decreases uniformly. The code of the image process and the model fit can be found on Zenodo (https://doi.org/10.5281/zenodo.6407198).

Text S4.

Dye release experiments with a side-looking camera were conducted to illustrate the vertical and streamwise migration of the dye plume in sediment bed (Fig. S11a). The solid fraction of vegetation is 0.05, and the velocity of overlying flow is 3.6 cm/s. Figs. S11b and S11c shows the distributions of fluorescence intensity in vertical and streamwise directions (along z-axis and x-axis), respectively. Fig. S11b shows that the region where fluorescence intensity exceeds 80% peak fluorescence intensity (between gray dash lines) does not expend during the first 2 hours of the experiment, suggesting the vertical migration of dye through the sediment is not significant. For the streamwise elongation of dye plume, the velocity of the dye front is 1.0~1.5% of the velocity of overlying flow to the downstream in the sediment. We noticed that the streamwise fluorescence intensity decreases uniformly when $t =$ 0.3-2 hours (Fig. S11d). It implies that the dye fluxes entered and leaved the analyzed area were similar in the sediment and the decrease in fluorescence intensity captured by the downward-looking camera was mainly due to the exchange of dye to the surface water. We fitted the data with the proposed model when the fluorescence intensity decreases uniformly to quantify the hyporheic exchange across the sediment-water interface.

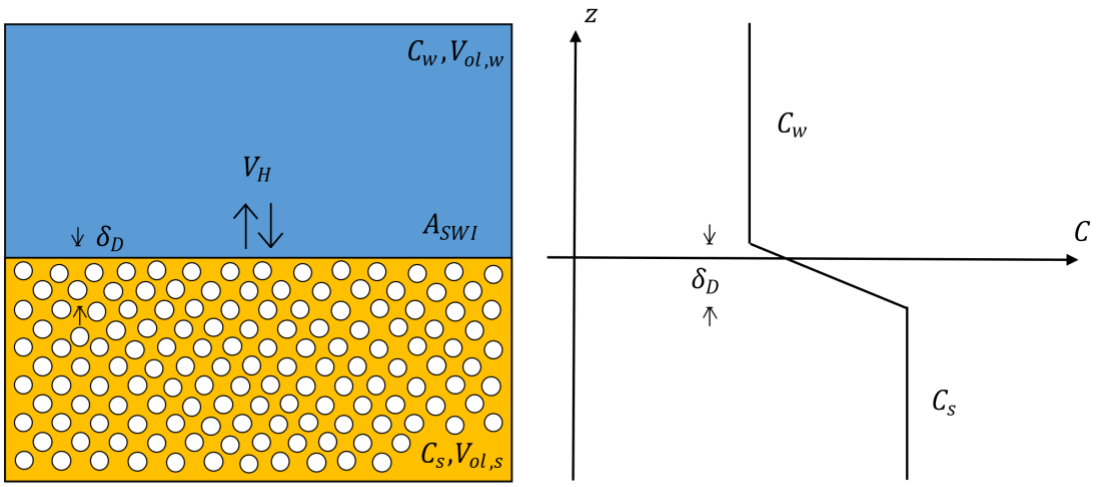

Figure S1. Schematic diagram of the proposed model. The blue and yellow area indicate the surface water and pore space in the sediment bed, respectively. C_w and C_s denotes the concentration of a solute in surface water and pore water within the sediment, respectively.

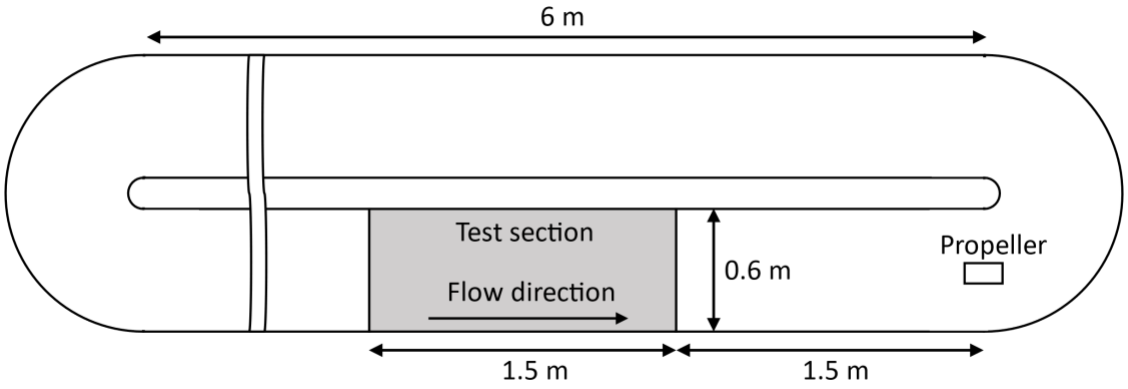

Figure S2. Schematic diagram of the race-track flume with a horizontal bed. The propeller was used to drive the flow.

Figure S3. The dropping system used to make hydrogel beads with controlled size. The polymer solution was poured into the cups and dropped into the 10 mM magnesium chloride solution in the container blow.

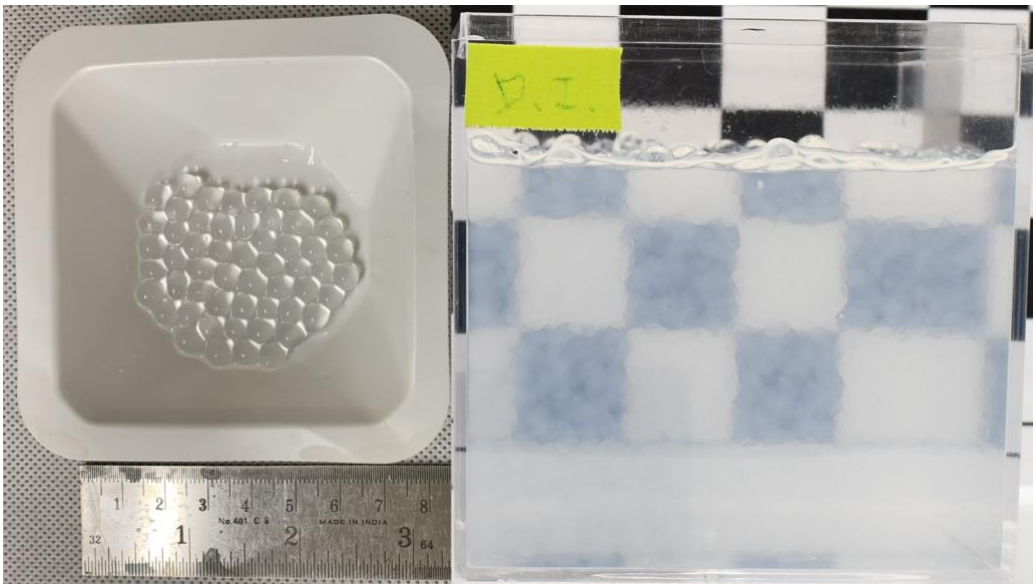

Figure S4. The hydrogel beads. The width of the container filled with hydrogel beads and water is 8 cm.

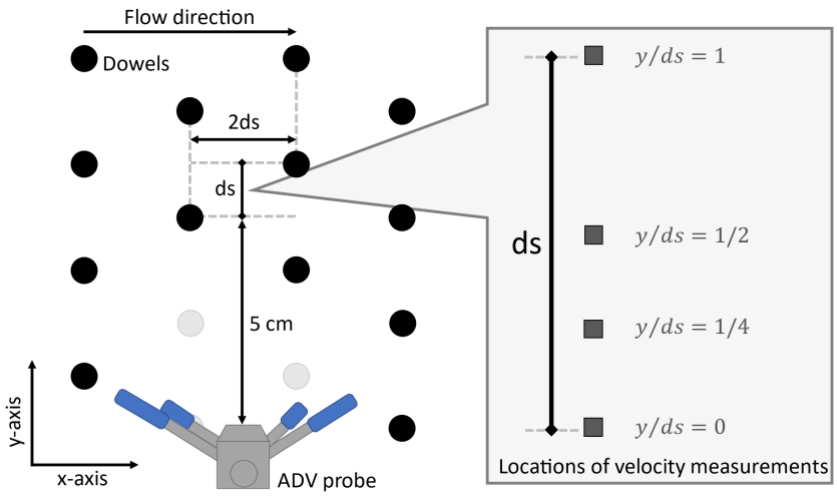

Figure S5. The locations of the velocity measurements for the vegetated cases using a side-looking Acoustic Doppler Velocimetry (ADV) in a flume with dowels (top view). The black circles represent vegetation dowels. The lateral center-to-center distance between two dowels 2*ds* = 2.6 cm. The square symbols indicate the locations of the velocity measurements relative to the vegetation dowels. Three dowels were removed to make space for the ADV probe (gray circles). The wake zones of the ADV probe did not affect the flow at measured locations. The measurements were taken at 64.0 cm downstream of the leading edge of the vegetation patch (in the middle of the test section). The vertical measured interval of each profile is 2.5 mm under 4 cm depth and 2-3 cm for the rest of the water depth. The distances between measured points and side wall are 300.0, 303.5, 307.0, and 314.0 mm, respectively. The spatially averaged velocity and the near-bed k_t was calculated using a spatial-average method justified in Yang et al. (2015) from local velocity and k_t at 4 locations. Specifically, the measurements at *y/ds* = 0, 1/4, 1/2, and 1 were weighted based on the lengths they cover along the transect of length *ds*, which are 12.5%, 25.0%, 37.5% and 25.0%, respectively. Yang et al. (2015) showed that the measurements at 4 representative locations relative to the upstream dowel are sufficient to obtain a converged result in channel with same model vegetation presented here. We further support this observation by showing that the differences between the mean flow velocity calculated from five profiles and four profiles are less than 5%.

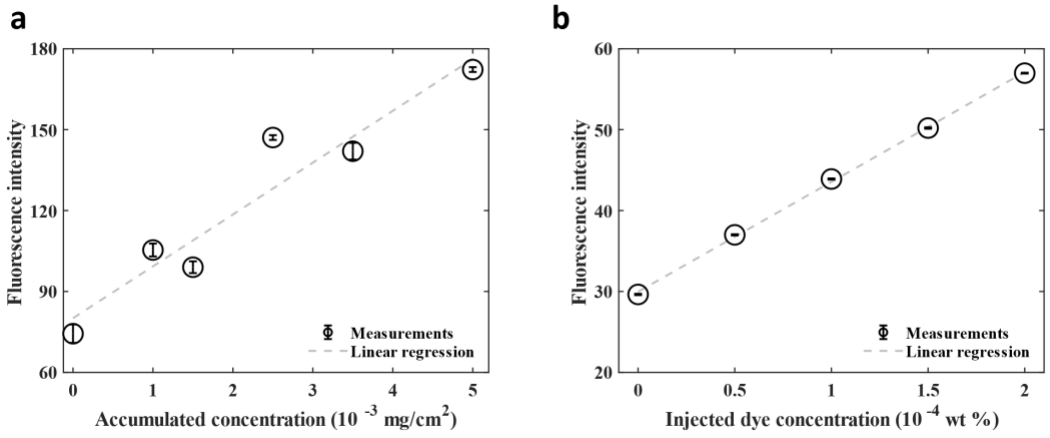

Figure S6. The linear relationship between injected dye concentration and fluorescence intensity detected by the downward-looking camera. (a) Dye calibration with a plastic box. The dashed line

represents the linear fit $y = 19.2x + 80.0$ with $R^2 = 0.91$. (b) Dye calibration with dye injection. The dashed line represents the linear fit $y = 13.6x + 30.0$ with $R^2 = 0.99$.

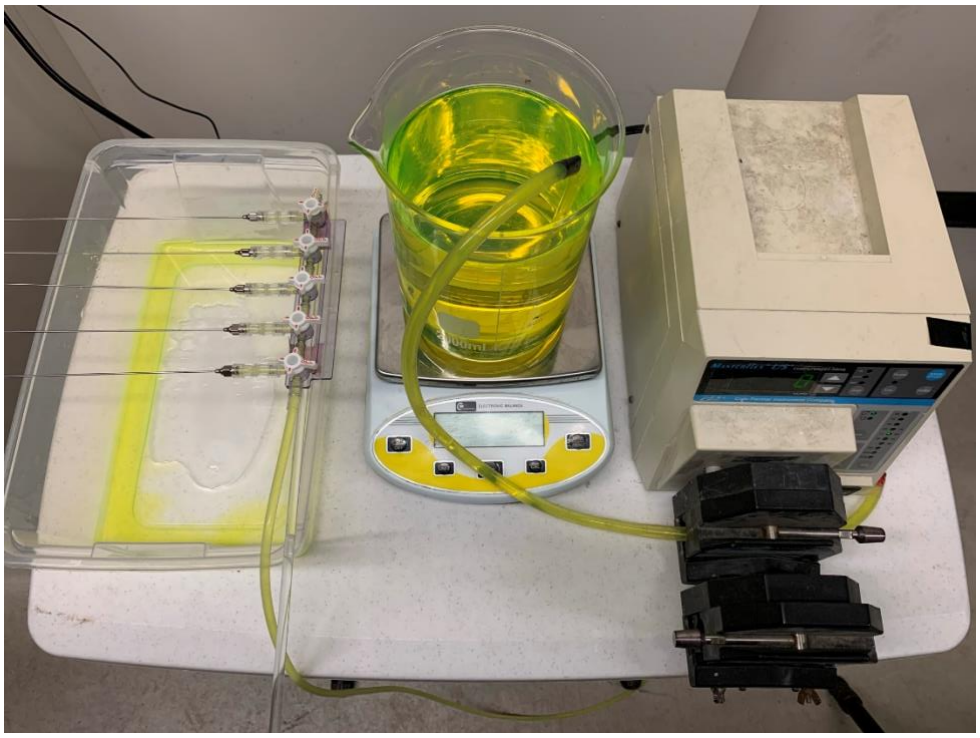

Figure S7. The dye injection equipment. A diverter was attached to five needles and a peristaltic pump. The amount of dye injected at each location was monitored by a scale during the injection process. Afterward, the total amount of injected dye was calculated from the weight of dye solution in the container before and after the dye injection.

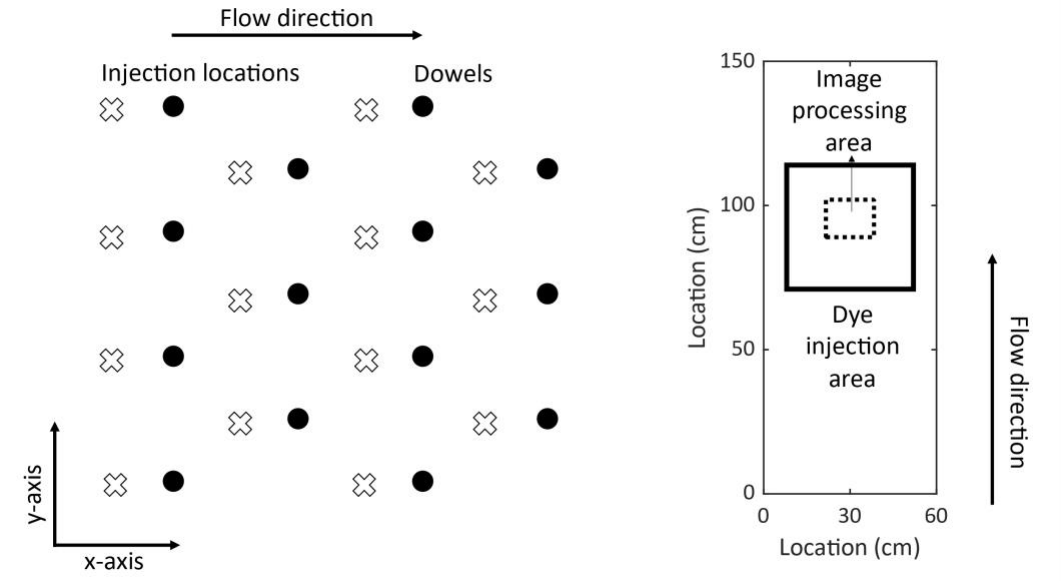

Figure S8. Location of dye injection. The left figure shows the dye injection locations relative to the dowl positions. The figure at right hand side shows the dye injection area (44 cm × 43 cm, thick solid line) in the test section and a smaller image processing area (22 cm × 17 cm, dash line).

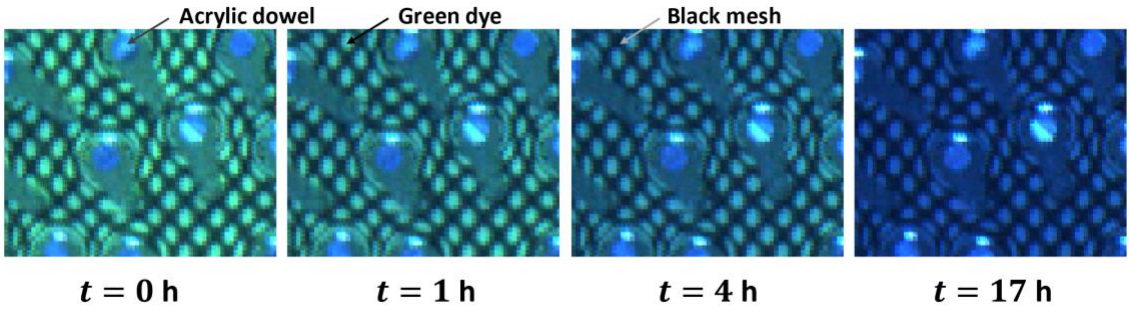

Figure S9. Images showing the decrease in the concentration of a fluorescent dye in the sediment over time during a dye release experiment. The dye, illuminated by a blue light lamp, emitted green light. The mean flow velocity of this case is 0.7 cm/s. Flow was started at t = 0 h.

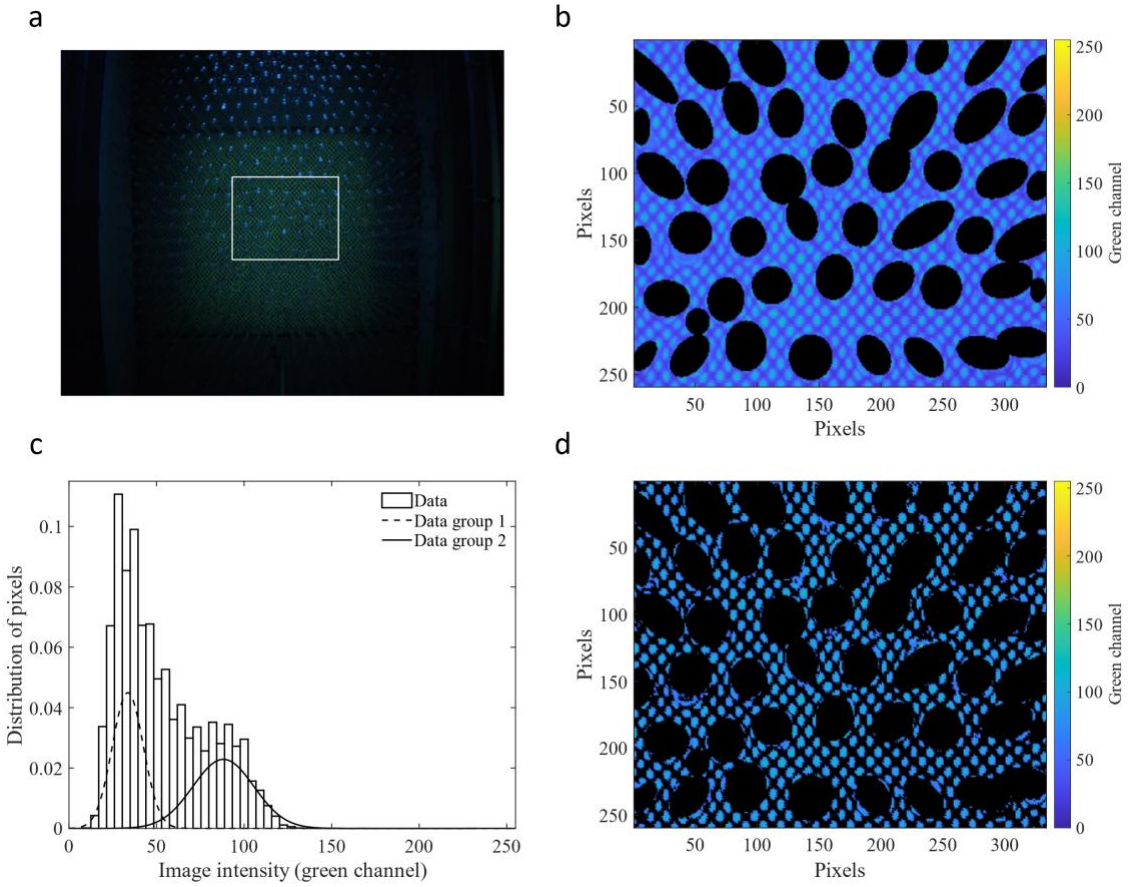

Figure S10. Image processing steps. (a) Crop the original image. (b) Remove the pixels occupied by vegetation dowels. (c) Separate pixels into two groups. (d) Locate the pixels occupied by hydrogel beads and pore water.

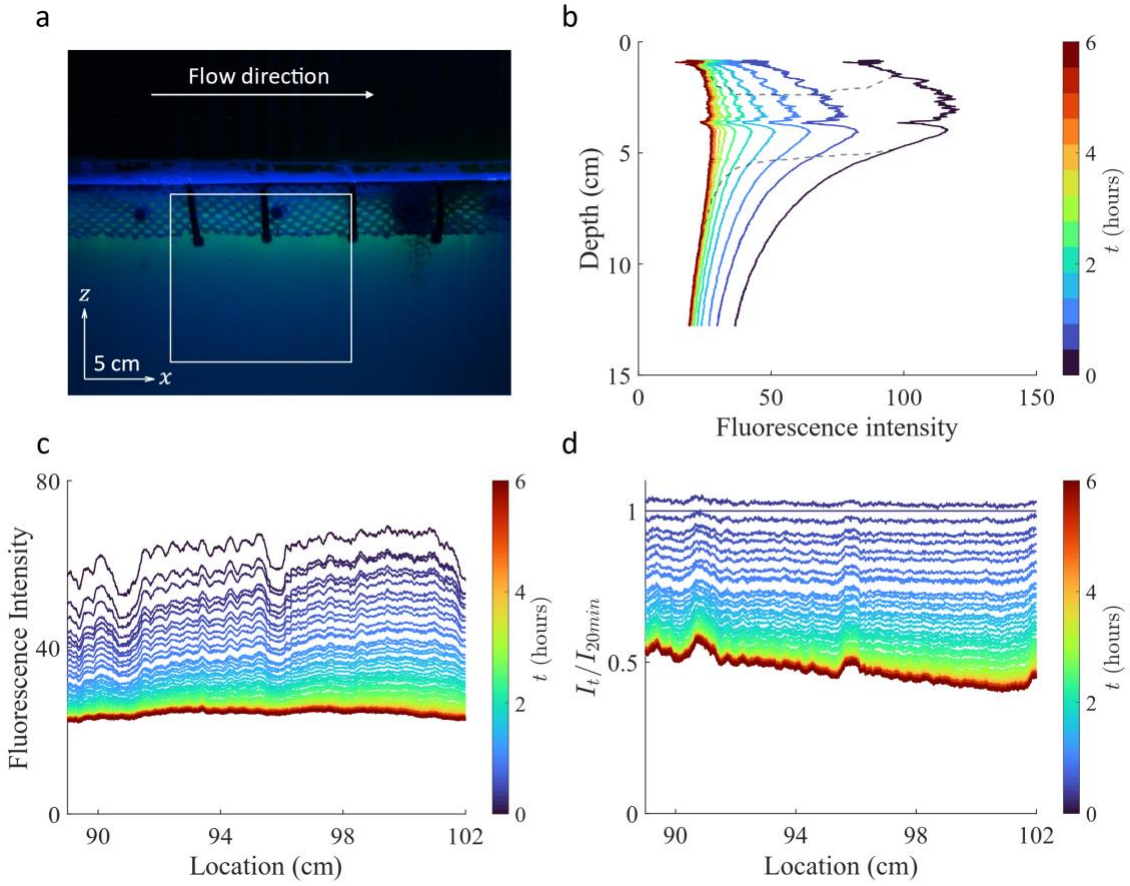

Figure S11. Dye release experiment captured by a side-looking camera. (a) The dye distribution at the beginning of the experiment. The fluorescent dye (green) was injected at 0 cm to 5 cm below the sediment surface. The fluorescence signal below 8 cm was due to the light scattered from above. The white box represents the region of interest used in the analyses. The left and right boundaries of the white box are also the boundaries of the region in the dye release experiments captured by a downward-looking camera (Fig S10a). (b) Vertical distribution of fluorescence intensity (averaged along *x*-axis). The line color presents experimental time with 30-minute intervals. Region between two gray dash lines show the region where fluorescence intensity exceeds 80% peak fluorescence intensity for each profile. (c) Streamwise distribution of fluorescence intensity (averaged along z-axis) with 5-minute time interval between lines. I_t stands for the fluorescence intensity at time *t*. (d) Streamwise profiles in (c) normalized by profile at t = 20 minutes.

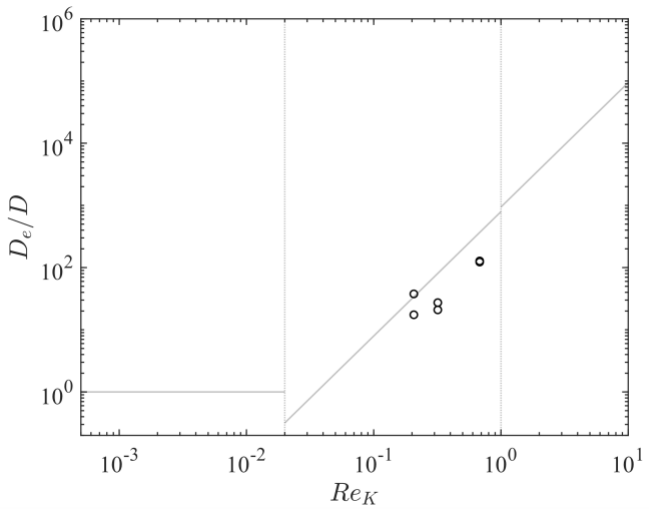

Figure S12. The normalized effective diffusion coefficient D_e/D and the permeability Reynolds number Re_K of cases without vegetation. D is molecular diffusion coefficient of 2.0×10^{-9} m^2/s when water is 20℃. $Re_K = K^{0.5}u_*/\nu$. K is the sediment permeability. u_* is the shear velocity and ν is the fluid kinematic viscosity. Effective diffusion coefficient D_e is evaluated by Eq. 20 of Grant et al. (2012). Gray lines are the interfacial transport model proposed by Voermans et al. (2018a). The circles are our measurements of the cases without vegetation. Note that the friction velocity used to calculate Re_K was estimated by fitting the vertical flow velocity profile with log velocity profile. The flow in the cases with mean flow velocity of 1.7 cm/s is transitional flow (Re = 1973) and its velocity profile doesn't follow log profile, thus, the friction velocities cannot be estimated, and the data are not shown in the plot.

Table S1. Flow conditions and effective diffusion calculated using 1D diffusion model of each case. Friction velocity u_* was estimated by fitting vertical velocity profiles with log profile. Vegetation Reynolds number Re_v was calculated with the modified vegetation-related hydraulic radius following Cheng and Nguyen (2011). Permeability Reynolds number Re_K and turbulent shear penetration depth δ_p were calculated using the formulated proposed by Voermans et al. (2018a). Effective diffusion coefficient D_e is evaluated by Eq. 20 of Grant et al. (2012).

	U [m/s]	u_* [m/s]	Re	${Re_v}^*$	${Re_K}^{**}$	${\delta_p}^{***}$ [m]	D_e [m^2/s]	V_H [m/s]
Cases without vegetation	0.017	-	1793	-	-	-	2.5E-08	7.2E-07
	0.017	-	1793	-	-	-	1.2E-08	1.2E-06
	0.040	0.0024	4344	-	0.21	0.00022	3.5E-08	1.8E-06
	0.040	0.0024	4344	-	0.21	0.00022	7.6E-08	1.1E-06
	0.066	0.0037	7107	-	0.32	0.00031	5.5E-08	1.4E-06
	0.066	0.0037	7107	-	0.32	0.00031	4.2E-08	1.4E-06
	0.154	0.0079	16524	-	0.68	0.00058	2.6E-07	4.1E-06
	0.154	0.0079	16524	-	0.68	0.00058	2.5E-07	3.8E-06
Cases with vegetation	0.007	-	844	471	-	-	1.9E-08	5.7E-07
	0.007	-	844	471	-	-	6.2E-09	5.5E-07
	0.016	-	1793	1002	-	-	4.6E-08	1.5E-06
	0.016	-	1793	1002	-	-	4.0E-08	1.3E-06
	0.024	-	2636	1473	-	-	8.5E-08	2.5E-06
	0.024	-	2636	1473	-	-	7.3E-08	2.7E-06
	0.036	-	4007	2239	-	-	1.6E-07	3.5E-06
	0.036	-	4007	2239	-	-	8.7E-08	4.0E-06

* $Re_v = Ur_v/\nu$, $where r_v = \frac{\text{water volume}}{\text{effective wetted area}} = \frac{8ds^2H}{3d_vH}$

** $Re_K = \sqrt{K}u_*/\nu$; K is the sediment permeability; u_* is the shear velocity and ν is fluid kinematic viscosity.

*** $(\delta_p u_*)/\nu \approx 8Re_K^{1.8}$.